



X-ray nanotomography analysis of the microstructural evolution of LiMn_2O_4 electrodes



Zhao Liu^a, Kai Han^{b, c}, Yu-chen Karen Chen-Wiegart^{d, e}, Jiajun Wang^d, Harold H. Kung^b, Jun Wang^d, Scott A. Barnett^{a, *}, Katherine T. Faber^{a, **}

^a Department of Materials Science and Engineering, Northwestern University, Evanston, IL, 60208, USA

^b Department of Chemical and Biological Engineering, Northwestern University, Evanston, IL, 60208, USA

^c College of Chemistry and Chemical Engineering, Central South University, Changsha, 410083, China

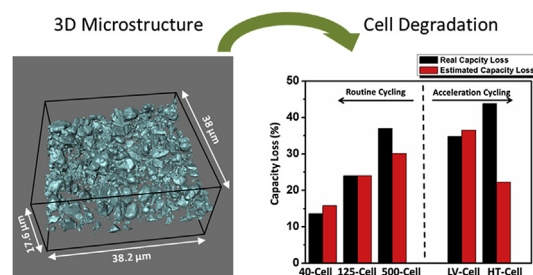
^d National Synchrotron Light Source II, Brookhaven National Laboratory, Upton, NY, 11973, USA

^e Department of Materials Science and Chemical Engineering, Stony Brook University, Stony Brook, NY, 11794, USA

HIGHLIGHTS

- X-ray nanotomography was used to analyze the 3D microstructures of LiMn_2O_4 electrodes.
- 3D images were statistically analyzed for homogeneity, surface area and size distribution.
- Cracks formed during electrode cycling were quantified via a dilation-erosion method.
- Mechanical cracking observed in cycled LiMn_2O_4 electrodes was correlated to capacity fade.
- Mn dissolution during cycling may explain capacity fade of high-temperature cells.

GRAPHICAL ABSTRACT



ARTICLE INFO

Article history:

Received 4 April 2017

Received in revised form

3 June 2017

Accepted 9 June 2017

Available online 17 June 2017

Keywords:

X-ray nanotomography

Lithium-ion battery

Cathode

Microstructural evolution

Quantitative analysis

ABSTRACT

One of the greatest challenges for advancing lithium-ion battery (LIB) technology is to minimize cell degradation during operation for long-term stability. To this end, it is important to understand how cell performance during operation relates to complex LIB microstructures. In this report, transmission X-ray microscopy (TXM) nanotomography is used to gain quantitative three-dimensional (3D) microstructure-performance correlations of LIB cathodes during cycling. The 3D microstructures of LiMn_2O_4 (LMO) electrodes, cycled under different conditions, including cycle number, operating voltage, and temperature, are characterized via TXM and statistically analyzed to investigate the impact of cycling conditions on the electrode microstructural evolution and cell performance. It is found that the number of cracks formed within LMO particles correlated with capacity fade. For the cell cycled at elevated temperatures, which exhibits the most severe capacity fade among all cells tested, mechanical cracking observed in TXM is not the only dominant contributor to the observed degradation. Mn^{2+} dissolution, as verified by detection of Mn on the counter electrode by energy dispersive spectrometry, also contributed. The current work demonstrate 3D TXM nanotomography as a powerful tool to help probe in-depth

* Corresponding author.

** Corresponding author. Current address: Division of Engineering and Applied Science, California Institute of Technology, Pasadena, CA 91125, USA.

E-mail addresses: s-barnett@northwestern.edu (S.A. Barnett), k-faber@northwestern.edu (K.T. Faber).

understanding of battery failure mechanisms, which could be applicable to electrode structure optimization for advancing LIB development.

© 2017 Elsevier B.V. All rights reserved.

1. Introduction

Lithium-ion battery (LIB) technology plays a key role in modern battery technologies, well developed and widely commercialized. However, one of the greatest challenges that limits its further development is long-term stability during cell operation. To overcome this challenge, it is essential to gain an in-depth understanding of battery degradation mechanisms [1,2]. In general, the electrode chemistry and microstructure of an LIB electrode continuously change during repeated operations of lithiation/delithiation [3]. Many processes contribute to cell degradation during repeated lithiation/delithiation [4–13]. For example, dissolution [7] and particle fracture/cracking [8–11] of the electrochemical active materials commonly accompany cell impedance increases that result in capacity fade. However, the correlation between the electrode microstructural evolution and battery electrode degradation is still not well substantiated due to the inadequate description and quantification of complex multi-scale electrode microstructures [14].

Three-dimensional tomographic techniques such as X-ray computed tomography (XCT) and focused ion beam-scanning electron microscopy (FIB-SEM) provide opportunities to gain quantitative insight into the three-dimensional (3D) LIB electrode microstructures at different length scales [15–25]. The collected 3D reconstruction data sets not only provide detailed information on electrode microstructure, but also serve as direct input for 3D simulations of the electrode processes [24,25]. Recently, both techniques have been used to study the 3D microstructural evolution of electrodes during cycling as well as structural changes on cell performance to probe cell degradation mechanisms [26–33]. Among these studies, materials with large volume changes during cycling have been characterized via *in situ* XCT to track electrode microstructural evolution during battery operation [26–29]. The *in situ* method provides the benefit of non-destructively tracking of electrode structure evolution in real time, thereby enabling direct correlation to battery performance. However, for intercalation-electrode materials where degradation typically involves changes occurring gradually over hundreds of cycles, it is not an ideal characterization method. The main reason is that radiation damage of the cells during long term cycling is not well understood and the measurement accuracy of both structural and electrochemical performance may be compromised by damage from the beam [30]. Therefore, *ex situ* measurement of multiple samples (from the same batch) under different electrochemical cycling conditions is an alternative to correlate electrode structural evolution with cell performance [31–33]. Under these circumstances, the electrochemical performance of the each cell is known with certain accuracy. However, previous studies on commercial cells show that one of the largest challenges in *ex situ* measurements is structural inhomogeneity, both cell-to-cell and spatial variations, that limits the capability to resolve the electrode structural changes on cycling [16]. A combination of well-controlled electrode processing procedures and designed electrochemical cycling conditions is essential to probe degradation mechanisms of cathode materials based on intercalation chemistry.

LiMn₂O₄ (LMO) is known as a favorable cathode material compared to other commercial cathodes (e.g. LiCoO₂), because of its

high power density, low cost, and environmental friendliness [34]. Previous studies show the capacity fading of cycled LMO cells could be qualitatively correlated to electrode structural degradation [5,13,35]. However, to date, a systematic quantification of how electrochemical cycling conditions impact the electrode 3D structure of LMO, and consequently the cell performance, is still not realized. The goal of this work is to demonstrate the use of *ex situ* transmission X-ray microscopy (TXM) nanotomography to relate 3D microstructural evolution to electrochemical performance of intercalation battery materials. *Ex situ* TXM nanotomography was applied to collect 3D data from LMO cells cycled with different operating parameters, including cycle number, temperature and operating voltage. Statistical analysis of electrode structural inhomogeneity was firstly conducted. Microstructural parameters, including surface area and particle size distribution, were then extracted from samples by 3D image analysis with different electrochemical conditions. Finally, the quantitative results were combined with fracture models and elemental energy dispersive spectrometry (EDS) analysis to assess the correlation between structural evolution and cell performance, providing a more comprehensive understanding of morphological evolution-induced battery degradation.

2. Experimental methods

2.1. LiMn₂O₄ electrode preparation

The lithium-ion battery electrode slurries were prepared by mixing LiMn₂O₄ (Sigma-Aldrich), polyvinylidene difluoride (PVDF, Sigma-Aldrich) and carbon black (TIMCAL, Super P) in a weight ratio of 70: 10: 20 in an *n*-methyl pyrrolidone solvent (NMP). First, the LiMn₂O₄ (LMO) and carbon black powders were mixed using a mortar and pestle for an hour to produce a homogeneous mixture of the active materials with carbon black. The NMP solution containing the PVDF binder (5%wt. PVDF in NMP) was then added to the mixture and stirred for ~2 h to form a homogeneous slurry. After mixing, the resulting slurry was cast onto aluminum foil (Alfa Aesar) using a notched bar with a 100 μm gap to form an electrode of uniform thickness [36]. The electrode was then transferred to the oven and dried at 120 °C for 2 h to evaporate the NMP. Finally the electrode was placed between two pieces of weighing paper and punched into 1.2-cm diameter electrode disks for the coin cell assembly.

2.2. Coin cell assembly and electrochemical measurement

Before cell assembly, the as-prepared electrode disks were first placed inside a vacuum oven at 120 °C overnight to remove any residual water arising from storage in air. The electrode was then transferred into a glove box and weighed with a microbalance. The mass of each electrode was measured five times to obtain an average value. The mass of the active materials was obtained by subtracting the mass of aluminum foil, and correcting for the fraction of active material in the mixture (70 wt.%). Coin cells (type 2016) were used to measure the electrochemical behavior of the LMO electrode with lithium metal foil as the counter electrode. The electrolyte was a solution of 1.2 M LiPF₆ dissolved in ethylene

carbonate/ethyl methyl carbonate (EC/EMC, 3:7, v/v, BASF, Germany) and the separator was a Celgard 2500 film (Celgard, US). All coin cells were assembled in an argon-filled glove box with both H₂O and O₂ concentrations less than 1 ppm.

Galvanostatic charge/discharge measurements were performed using a NEWARE BTS-5V/5 mA battery test station (NEWARE Co. Ltd. Shenzhen, China) at a cycling rate of 1C, in which the constant cycling current was programmed to charge/discharge the cell in 1 h based on its theoretical capacity. Three cell-cycling parameters – number of cycles, operating voltage, and operating temperature – were investigated to assess how electrochemical cycling influenced electrode microstructure and capacity loss, as specified in Table 1. In order to investigate the impact of number of cycles (routing cycling), three cells were cycled under standard conditions, specifically, room temperature, voltage range of 3.4 V–4.45 V (vs. Li⁺/Li), for 40 cycles, 125 cycles, and 500 cycles. These cells are referred to as “40-Cell”, “125-Cell”, and “500-Cell,” respectively. One cell, labeled “LV-Cell”, was cycled 40 times at room temperature in the voltage range of 3.0 V–4.45 V (vs. Li⁺/Li) to investigate the effect of operating voltage. The lower cut-off voltage of 3.0 V was close to that which triggers the onset of the Jahn-Teller distortion (2.96 V) [37]. Finally one cell, “HT-Cell,” was operated in the standard voltage range but cycled at a higher temperature (55 °C) to examine how operating temperature impacts cell degradation. These accelerated cycling conditions in LV-Cell and HT-Cell – lower cut-off voltage and higher temperature respectively – were purposely introduced to study the degradation under accelerated cycling. After cycling, all cells were carefully disassembled in the glove box in their discharged state. The LMO cathodes and lithium metal anodes were then detached from the separator, and dried in the glove box before further structural and chemical characterization.

2.3. TXM nano-tomography

Two fresh and the five cycled LMO cathodes listed in Table 1 were studied via full field transmission X-ray microscopy (TXM) at beamline X8C, National Synchrotron Light Source, Brookhaven National Laboratory. Because the as-obtained electrode thickness was less than 40 μm, it was possible to prepare for TXM by cutting a wedge-shaped sample from the cathodes using a sharp razor blade, which is a suitable method for thin (<40 μm) electrode samples and is much less time-consuming than the FIB lift-out technique applied in, e.g., thicker electrodes in batteries and solid oxide fuel cells [38]. Fig. 1 (a) shows the scanning electron microscopy (SEM) image of a wedge-shaped fresh electrode sample. The overall sample dimension was kept within the 40-μm field of view to ensure good data quality from the tomographic data reconstruction. The sample was then mounted onto a tungsten pin with epoxy resin. Fig. 1(b) shows the 2D mosaic radiograph of the sample highlighting the region used for 3D tomography data collection. A portion of the electrode (highlighted with a red rectangle) was within the field of view, which was necessary for high quality image reconstruction. Incident X-ray energy of 8300 eV was used to provide image contrast between active and non-active phases. Each tomographic data set was collected with 1001 projections over the

angular range of 180° with a field of view of 40 × 40 μm² that had a voxel size of 38.9 nm (the 2 k × 2 k CCD camera binned into 2 × 2 pixels). A standard filtered back-projection algorithm was used to reconstruct the 3D volume. Fig. 1(c) shows a representative virtual cross-section of the fresh LMO sample from 3D reconstruction, where a layer of LiMn₂O₄ particles (light gray) covered the aluminum current collector. Note that, because the non-active phases, including carbon and binder, had little X-ray absorption under the prescribed measurement conditions, there was no contrast to differentiate them from the electrode porosity. The as-collected reconstructed 2D images were then segmented via Otsu's algorithm [39]. The noise filter built in ImageJ (National Institutes of Health, MD, USA) was used on images that needed further noise reduction and artifact removal [40,41]. The segmented images were then imported into Amira 5.5.0 (FEI Visualization Sciences Group, MA) for 3D visualization, as shown in Fig. 1(d).

2.4. Microstructural quantification

In this study, specific surface area (S_A) and particle size distribution (PSD) of the LMO phase were quantified and analyzed for all electrode samples. The total surface area of the LMO phase was calculated via the Marching Cube algorithm based on the segmented data [42]. The S_A was then determined by normalizing the total surface area with its corresponding phase volume. One possible structural change that might occur on battery cycling was cracking of LMO particles [5,13]. The quantity of cracks in the electrodes could be evaluated based on specific surface area, where higher crack density in the electrodes should correspond to higher specific surface area relative to a crack-free material. However, because the specific surface area is also influenced by particle size, i.e., sample to sample variation, S_A alone may be ineffective in resolving microstructural changes among cycled samples. In order to quantitatively analyze the crack surface area formed during cycling, an image processing method, namely a dilation-erosion process, was further introduced to resolve the specific surface area contribution from the cracks formed during cycling. The dilation operation on the binary image enlarges the boundaries of the region of interest, while the erosion operation erodes away the boundaries of the same region [44]. In the current study, both dilation and erosion were performed on 3D TXM nanotomography data using ImageJ. For each data set, to remove all cracks which appeared in the 3D volumes, the volumes were dilated and eroded by two voxels via ImageJ. Fig. S1 illustrates the process of removing cracks using dilation-erosion. First, the LMO phase was dilated to make sure the cracks in the electrodes are removed. Then the erosion operator was applied to remove the extra material on the particle boundary generated by dilation. As shown in Fig. S1, cracks were effectively removed with other regions remaining nearly unchanged after dilation-erosion. The surface area contributions (ΔS_A) from the cracks were then calculated from the difference between specific surface area before and after the dilation-erosion process. Finally, for particle size distribution calculations, the method introduced by Holzer et al. was used [43].

2.5. SEM and EDS analysis

The electrode samples that were characterized via TXM nano-tomography were also characterized with scanning electron microscopy (Hitachi SU8030 was operated at 10 kv) to acquire more detailed information on the morphology of LMO particle surface. All cycled electrodes were washed with dimethyl carbonate (DMC) to remove any electrolyte residue on the sample before characterization. Furthermore, in order to probe the possibility of the

Table 1
Designed experiments for LMO coin cells.

Sample name	Number of cycles	Voltage	Operating temperature
40-Cell	40	3.4 V–4.45 V	Room Temperature
125-Cell	125	3.4 V–4.45 V	Room Temperature
500-Cell	500	3.4 V–4.45 V	Room Temperature
LV-Cell	40	3.0 V–4.45 V	Room Temperature
HT-Cell	40	3.4 V–4.45 V	55 °C

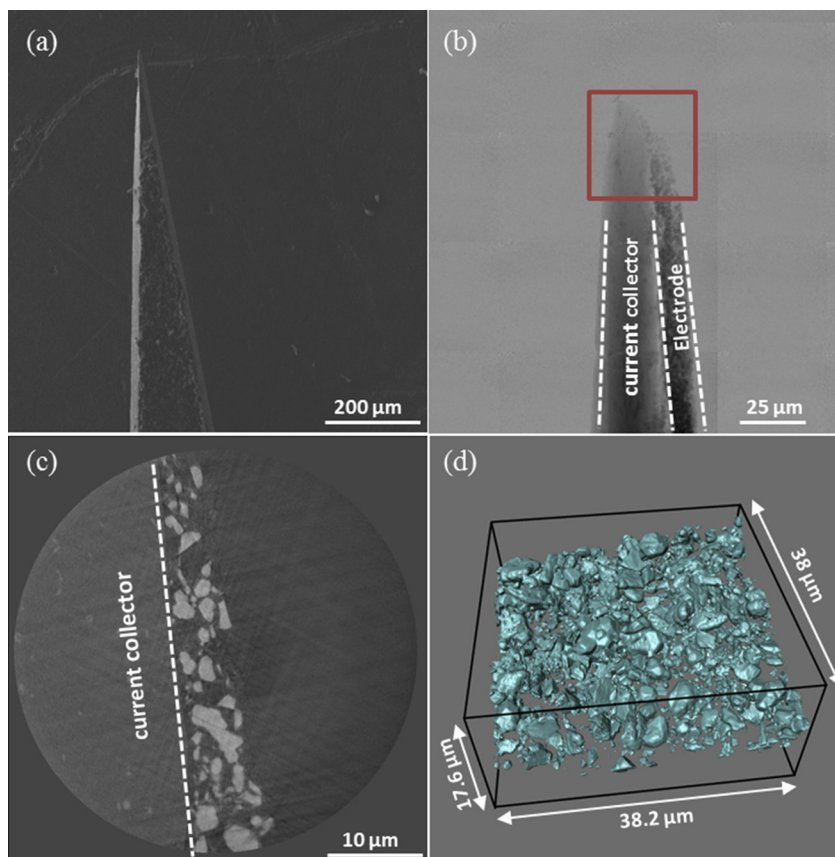


Fig. 1. (a) SEM image of a wedge-shaped fresh electrode sample cut with razor blade. (b) 2D mosaic radiography image of the sample highlights the region for data collection. The red rectangle shows the size field of view under TXM during data collection (c) A virtual cross-section from TXM tomography reconstruction of fresh electrode sample. (d) 3D reconstruction of LiMn_2O_4 phase in a fresh cathode. (For interpretation of the references to colour in this figure legend, the reader is referred to the web version of this article.)

dissolution of active materials and migration of dissolved Mn^{2+} ions during cycling, the anodes (lithium metal) used to cycle against LiMn_2O_4 electrodes from the HT and 40-cycle cells were analyzed via energy dispersive X-ray spectroscopy (EDS).

3. Results and discussion

3.1. Electrochemical performance

Fig. 2 shows the discharge capacity of the first and final cycle for each cell. All cells operated at room temperature delivered ~ 70 mAh/g discharge capacity in the first cycle at 1C. Fig. S2 shows a representative charge and discharge curve of the LMO cells (LV-Cell). That similar discharge capacities were observed for all samples except the HT-Cell in the first cycle confirmed sample uniformity within a given batch, a prerequisite to correlate structural changes with cell performance. The HT-Cell, which was cycled at 55°C , demonstrated inferior first-cycle discharge capacity. Blyr et al. suggest that the substandard electrochemical performance was mainly due to instability of LiMn_2O_4 at high temperatures, when Mn^{2+} dissolution into the electrolyte was enhanced, even at the initial stage of discharge [45]. The capacity loss of each cell is shown in Table 2, and it is defined as:

$$\text{Capacity Loss} = \frac{Q_{\text{initial cycle}} - Q_{\text{end cycle}}}{Q_{\text{initial cycle}}} \quad (1)$$

where Q is the discharge capacity. For cells operated under standard conditions, the capacity loss increases with cycle number,

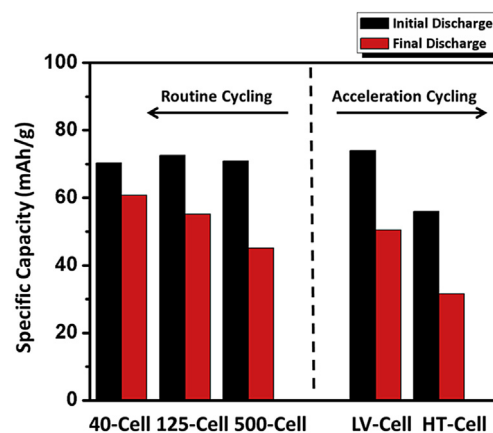


Fig. 2. Specific capacity of first and final cycle of each cell listed in Table 1.

leading to $\sim 40\%$ capacity loss after 500 cycles. For cells cycled under a lower cut-off discharge voltage and at high temperature, accelerated cell degradation was observed within the first 40 cycles. The LV-cell demonstrated more than 30% capacity loss while the HT-cell cycled at 55°C lost nearly 45% of its original capacity, even more than cells after 500 cycles under standard conditions. The following analysis focuses on quantifying microstructural changes under different cycling conditions so as to derive connections between electrode structure changes and capacity loss.

Table 2
Calculated capacity loss of each cell.

Sample name	Capacity loss (%)
40-Cell	13.6%
125-Cell	24%
500-Cell	37%
LV-Cell	31.8%
HT-Cell	43.8%

3.2. TXM nanotomography

Fig. 3 shows representative 2D reconstructed virtual slices of each electrode sampled using TXM nano-tomography. Clear contrast was achieved between LiMn_2O_4 particles (light gray) and the other electrode components (dark gray) including carbon, binder and porosity. Fig. 3 (a) – (c) reveal the electrode microstructural evolution with increased cycle number. Compared to the fresh electrode, cracks were generated in particles during cycling. The cracks in cells that operated under standard condition were stress induced via a combination of composition gradients and a first-order phase transformation [9–11]. For cells operated in the range of 3.4 V–4.45 V, the lithium extraction/insertion resulted in isotropic contraction and expansion of the cubic structure. In prior studies, cubic $\text{Li}_x\text{Mn}_2\text{O}_4$ spinel was cycled between 4.45 V and 3.4 V, corresponding to a variation in the composition range of $0.2 \leq x \leq 1$, and experienced a 6.5% volume change [37,46]. At 4 V, lithium was removed from the solid solution of $0.5 \leq x \leq 1$ and the composition gradient-produced stress was capable of fracturing particles. For $x \leq 0.5$, a first-order cubic-to-cubic phase transformation resulted in a misfit strain of 1.2% between the coexisting cubic phases, which induced particle fracture [10]. It appears that the crack formation could be one of the mechanisms for the observed capacity loss; small particles formed by fracture may lack contact with the carbon particle network and become inactive since they cannot access electrons needed for the electrochemical reaction.

Fig. 3 (d) – (f) compare the microstructure of electrodes after 40 cycles under different electrochemical cycling conditions. It is apparent that, with identical numbers of cycles, the lower discharge cut-off voltage of 3.0 V resulted in more severe cracking. The severe cracking found in this sample could be explained mainly by the onset of the Jahn-Teller effect, where the distortion of MnO_6 octahedra causes 12% shrinkage along the c axis, 3% expansion along the a axis, and 16% change in the c/a ratio; the overall volume change is 6.6% [13]. The abrupt lattice parameter changes associated with the cubic-to-tetragonal phase transformation is expected to give rise to larger stresses than those induced due to isotropic expansion and cubic-to-cubic phase transformation during the electrochemical cycling at 4 V [47]. It is noted that, although the discharge voltage for all cells was above the onset of the Jahn-Teller distortion (2.96 V), the cell discharged to 3 V was more vulnerable to this crystallographic damage because it occurred under dynamic, non-equilibrium conditions [48]. Although the HT-Cell that displayed the fastest capacity fade, the amount of particle fracturing was similar to the 40-Cell. This might indicate that, for high temperature cycling, other processes besides particle fracture are the main contributors to cell degradation.

3.3. Microstructure quantification

Microstructure analysis was performed to quantitatively correlate the electrode morphological changes with cell performance using two methods. First, because the specific surface area (SA_S) can denote microstructural changes including cracking or surface roughening caused by material dissolution, this parameter was used to analyze the impact of different cycling conditions on electrode microstructural changes. Since sample-to-sample variation may produce misleading results in direct comparison of SA_S results, the cluster sample scheme, which considers each electrode sample as a cluster of voxel elements, was used to statistically analyze the SA_S extracted from the 3D reconstructions (See supplemental information for statistical assumptions and analyses) [16]. Table 3

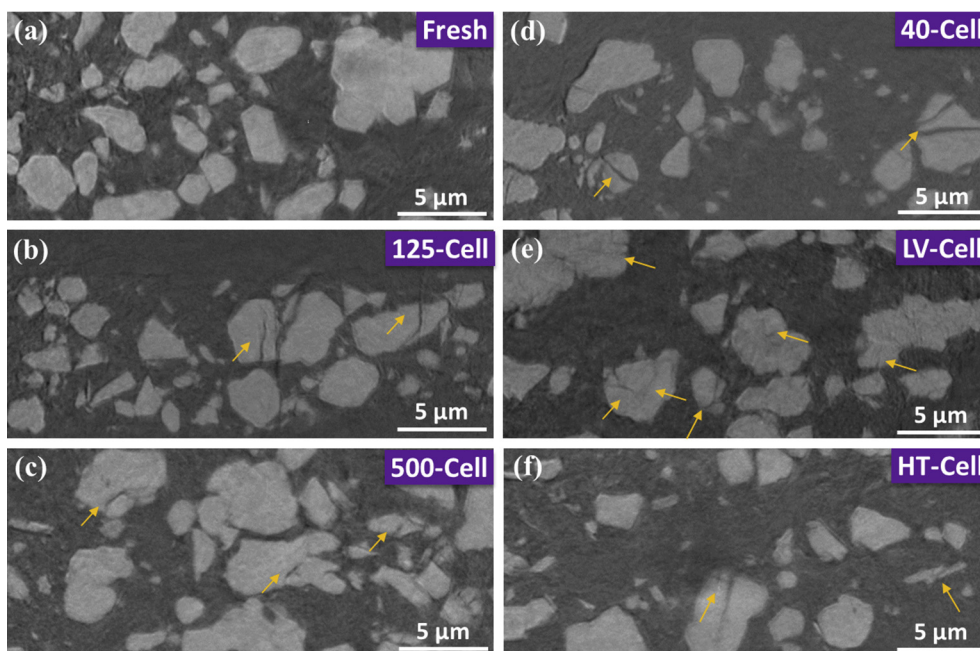


Fig. 3. Representative 2D virtual slices of electrodes from X-ray nanotomography reconstructions. (a) Fresh, (b) 125-Cell, (c) 500-Cell, (d) 40-Cell, (e) LV-Cell, and (f) HT-Cell. Arrows in the image point to cracks within LMO particles.

summarizes the specific surface area results. Two fresh 3D data sets were used to evaluate the structural homogeneity resulting in an average value SA_S of $3.55 \mu\text{m}^{-1}$ with a standard error of $0.05 \mu\text{m}^{-1}$. SA_S for all cycled samples showed an increase of specific surface area, which required validation by cluster sampling.

For the measured standard error of approximately 1.4% for the fresh electrodes, and considering that all electrodes were from the same batch, only one cluster was chosen for each LMO cell with different cycling conditions. In order to estimate the standard error for each of the cycled samples, we assumed that SA_S variances of fresh versus cycled samples were equal. A one-tailed Z-test was conducted with the null hypothesis, H_0 , that the SA_S was the same between the fresh and cycled cathodes. The alternative hypothesis H_1 was that SA_S of the cycled cathode was larger than that of the fresh cathode. The P-values (a value that describes the probability of the H_0 statement, namely SA_S is the same between the fresh and cycled cathodes, is true) obtained from the analyses are compiled in Table 3. All P-values were smaller than 0.001, from which we concluded that cycling can result in significant changes in SA_S with more than 99.9% confidence. The statistical analysis validated that the increase of the SA_S correlated well with cell degradation. Moreover, it suggested that in a system with homogeneous microstructures, *ex situ* measurement methods combining statistical analysis of 3D data and electrochemical cycling data can be used to build microstructure-performance correlations.

Although it was possible to differentiate microstructural distinctions between fresh and cycled electrodes through statistical analysis, no difference beyond statistical error could be identified among cycled electrodes. In order to evaluate the contribution of cracking to SA_S , the second method, the dilation-erosion process, described earlier, was employed on the 3D tomographic data sets for each electrode under different cycling conditions [44]. SA_S was calculated before and after performing dilation-erosion process and the differences were defined as ΔSA_S , which is considered as the surface area contribution from crack formation during cycling. Dilation of the oxide particle boundaries by a few voxels effectively overlapped narrow cracks; subsequent erosion by the same number of voxels brought the boundaries back to their original positions, except that the narrow cracks were removed. Thus, dilation-erosion effectively removed cracks while retaining other features, e.g. the general particle shape remained unchanged (Fig. S1). Thus, any differences in SA_S (ΔSA_S) could be attributed to cracks.

Table 4 compiles the ΔSA_S results, where ΔSA_S for the fresh electrode was $0.04 \mu\text{m}^{-1}$. Because no cracks were observed in the fresh LMO particles from TXM data, this value could be considered the error associated with this image processing procedure (e.g. two particles which are in close proximity may be considered “cracks” that are removed during dilation-erosion). Based on the cluster sampling scheme, a one-tailed Z test was performed to statistically analyze crack formation differences between samples with the null hypothesis, H_0 , that ΔSA_S was the same between pairs of cycled cathodes. The alternative hypothesis H_1 was that ΔSA_S of a cell

cycled under one condition differed from that of a cell cycled under other conditions. Both H_0 and H_1 hypotheses are listed in Table 4 along with P-values obtained from the analyses. All P-values were smaller than 0.05, from which we conclude that for electrodes cycled under standard conditions, ΔSA_S increased significantly with cycle number with more than 95% confidence, and at magnitudes that far exceeded the imaging processing error ($0.04 \mu\text{m}^{-1}$). More cycles produced more cracks or greater crack area that correlated with continued cell degradation. Note that repeated electrochemical cycling requires the propagation of a phase boundary, and continued generation of cyclic stresses that may result in more cracks appearing in the more cycled sample (Table 4).

The LV-Cell has the largest ΔSA_S suggesting the most severe cracking among all cycled cells. Compared to the cell cycled under standard conditions for 40 cycles, the low voltage cycling cell shows significant increase of cracking with more than 95% confidence. The additional cracking was likely due to the stress generated via the Jahn-Teller distortion. Hence, in LMO, a slight increase in the discharge cut-off voltage above that for the onset of the Jahn-Teller distortion should significantly reduce cracking-induced battery degradation. For the cell operated at 55°C , which showed the most severe capacity loss, however, ΔSA_S was significantly lower than that associated with the LV-Cell. This indicated that, although the cracking resulted in capacity loss in this cell, it was not the only determining factor for degradation, and other mechanisms need to be considered, e.g. dissolution of the electrode components.

Fig. 4 shows LMO particle size distributions (PSDs) of fresh and cycled electrode samples. The fresh electrode had the largest median particle size ($1.04 \mu\text{m}$) and the LV cell had the smallest size ($0.77 \mu\text{m}$). Because the PSD algorithm based on the Holzer's method can effectively detect microstructural characteristics [43], such as cracking, the PSD of the LV cell further confirmed that it had the most cracks generated among all cycled cells. The PSDs of other cycled cells were comparable with each other but different from the fresh electrode.

3.4. SEM and EDS analysis

Although X-ray nanotomography provided quantitative insight into electrode microstructure changes during cycling, particle fracture during cycling did not fully explain the most severe electrode degradation observed in the HT-Cell. SEM and energy dispersive X-ray spectroscopy (EDS) were performed to provide further insight into the electrode degradation mechanism, especially for the HT-cell. Fig. 5 exhibits SEM images of the various cycled electrode microstructures. Consistent with X-ray nanotomography observations, when comparing the cells cycled for 40 cycles (Fig. 5 (e) and (f)), the LV-Cell was found to have the most severe cracking. Besides cracking, another significant microstructural difference was the nanometer-scale surface roughness (also see Fig. S3, the surface morphology comparison between HT-Cell and 40-Cell at high magnification) found on the HT-Cell surface, which was not well characterized via TXM nanotomography due to its limited resolution. This specific surface morphology indicated enhanced etching due to a parasitic electrode-electrolyte reaction and Mn^{2+} dissolution. It has been reported that dissolution of spinel electrodes in acid from the Li-based electrolyte at the sample surface resulted in capacity fade [45].

EDS was performed on the harvested lithium metal of the HT-Cell and 40-Cell to probe for the presence of manganese deposition from dissolved cathode. Fig. 6 shows the elemental analysis of the Li anodes after cycling, and the insets are SEM images of the corresponding region over which the EDS data were collected. Carbon (C) and oxygen (O) found on the used anode were from electrolyte residue and from the reaction between lithium and air

Table 3
Statistical analysis results of the total SA_S from 3D reconstructed LiMn_2O_4 data sets.

	SA_S (μm^{-1})	Standard error (μm^{-1})	P-value
Fresh electrode#1	3.59		
Fresh electrode#2	3.49		
Fresh electrode average	3.55	0.05	
40-Cell	3.97	0.05	<0.001
125-Cell	3.93	0.06	<0.001
500-Cell	3.88	0.06	<0.001
LV-Cell	4.07	0.04	<0.001
HT-Cell	3.85	0.04	<0.001

Table 4
Statistical analysis of the change in specific surface area, ΔSA_S , namely surface area contributed by crack formation during cycling, obtained by performing dilation-erosion on 3D data sets.

	ΔSA_S (μm^{-1})	H_0 for ΔSA_S	H_1 for ΔSA_S	P-Value
Fresh electrode#1	0.04			
40-Cell	0.21	40-Cell = Fresh electrode	40-Cell > Fresh electrode	<0.05
125-Cell	0.34	125-Cell = 40-Cell	125-Cell > 40-Cell	<0.05
500-Cell	0.45	500-Cell = 125-Cell	500-Cell > 125-Cell	<0.05
LV-Cell	0.58	LV-Cell = 40-Cell	LV-Cell > 40-Cell	<0.05
HT-Cell	0.31	HT-Cell = LV-Cell	HT-Cell < LV-Cell	<0.05

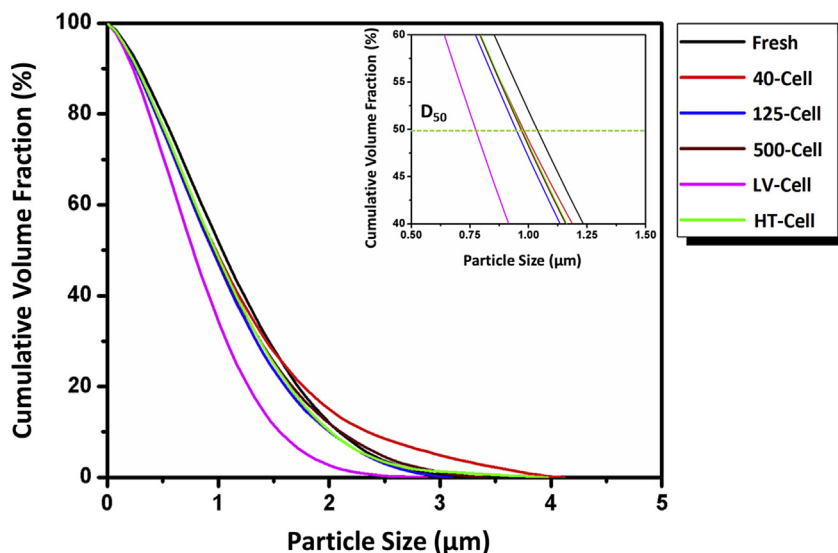


Fig. 4. Particle size distributions of fresh and cycled samples. Inset is an enlarged area highlighting the region near D_{50} .

during transfer of the sample to the SEM chamber. Phosphorus (P) and fluorine (F) were from the Li salt (LiPF_6) in the electrolyte. The Mn elemental signal was detected only on the anode cycled with LiMn_2O_4 at high temperature. Because both cells were operated for 40 cycles, these results suggested more severe dissolution of active materials at the higher temperature. Hence, Mn^{2+} dissolution was another degradation mechanism contributing to the capacity loss in the HT cell.

3.5. Fracture stress evaluation and crack density-performance correlation analysis

By extracting the microstructural parameters from the 3D reconstruction volumes of the electrodes, the mechanical behavior of LMO particles under different electrochemical cycling conditions can be interpreted using the Griffith criterion to assess the critical condition for cracking of LMO [49]. The critical fracture stress σ_{cr} required for crack growth can be obtained via:

$$\sigma_{cr} = \frac{\pi}{2} \sqrt{\frac{2E\gamma}{\pi a}} \quad (2)$$

where E is the Young's modulus, γ is the surface energy and a is the crack radius within the particle. Young's modulus of $E = 200$ GPa and surface energy of $\gamma = 0.58$ J/m² were used for the calculation [10,11,50], and we assumed that cracks found on LMO particles were semicircular surface cracks with a diameter $2a$. We further assumed that ΔSA_S contributed only from cracks formed during

cycling, which was validated by the TXM and SEM results shown in Figs. 3 and 5, and showed that most cracks propagated only partway through the particles. The crack radius a was estimated from ΔSA_S . First, the average particle size, obtained from the PSD calculation (Fig. 4), was used to calculate the number of particles in each reconstruction volume. Then, ΔSA_S was converted to crack surface area per particle by equating $\Delta SA_S/\text{number of particles}$ to πa^2 . Because it was assumed that each particle in the reconstruction volume had one crack, the as-obtained crack size represented the lower bound. The assumption that all particles had a crack was reasonable since the particle sizes were all above the size where LMO particles could fracture, according to Woodford et al. [10]. Table 5 lists the average crack radius, a , for each cycling condition and the stresses needed for further crack growth. The average crack length increased with the cycle number, and therefore lower critical stresses were required for further crack propagation as cycling continues. The LV sample required the least stress for further cracking. Since the critical stress for particle fracture decreases during cycling, cracking is expected to be more prevalent as cycling proceeds, and is most severe in the LV sample. Critical fracture stresses calculated here agree with the simulation results obtained previously [11,51,52].

It is possible that stresses below σ_{cr} might result in crack growth due to fatigue and/or chemical reaction at the crack tip. An in-depth understanding of the mechanical behavior of LMO electrode during cycling can be further addressed by using the as-obtained 3D microstructural reconstructions as input for 3D model simulations.

Because crack generation for each electrochemical cycling

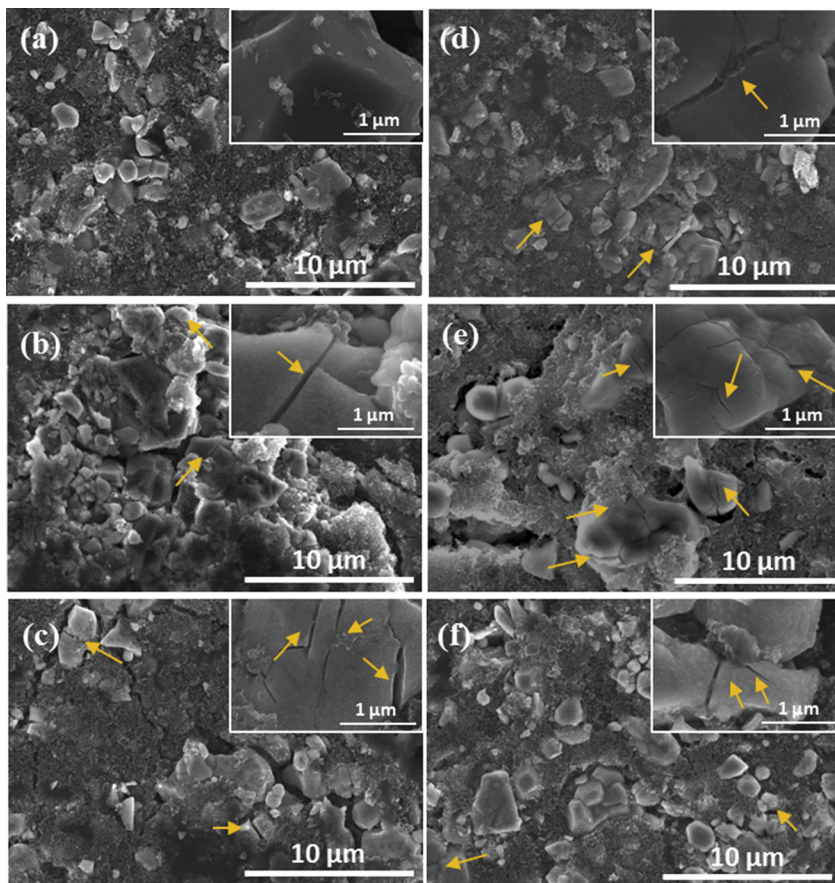


Fig. 5. SEM images of electrode structures of (a) fresh electrode, (b) 125-Cell, (c) 500-Cell, (d) 40-Cell, (e) LV-Cell, (f) HT-Cell. The insets are high-resolution images that exhibit detailed morphology of the surface of a single particle. Arrows point to the cracks that have intersected the surfaces of particles.

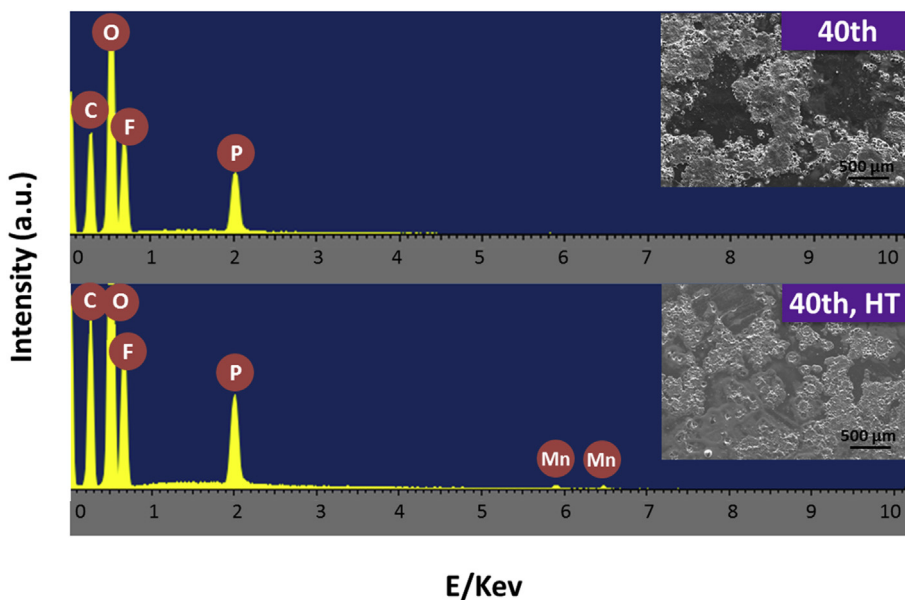


Fig. 6. EDS analyses of the harvested lithium metal anode of the 40-Cell (top panel) and HT-Cell (bottom panel). Insets are SEM images of the regions where data were collected.

condition was quantitatively resolved, the correlation between cracks produced during cycling and capacity fade was explored to further understand degradation mechanisms in each electrode. We assumed that the particle fracture will generate new particles that

were electrochemically inactive. By calculating the new particle formation of each cell, the capacity loss could be estimated and compared with the real capacity loss during cycling. The average particle size d can be calculated via:

Table 5
Crack length and critical fracture stress of LiMn₂O₄ electrodes.

	Crack size, a (μm)	σ_{cr} (MPa)
40-Cell	0.19	987
125-Cell	0.24	875
500-Cell	0.27	816
LV-Cell	0.31	766
HT-Cell	0.23	895

$$d = \frac{\varepsilon C}{SA_S} \quad (3)$$

where ε is the solid volume fraction, and C is the shape factor. During cell cycling, the particle cracking increases SA_S (for the cycled sample, SA_S is the sum of fresh electrode SA_S and ΔSA_S), decreases the particle size d , while the total solid volume V_P is constant. Therefore, the number of particles per unit volume, N_P also increases:

$$N_P \propto \frac{V_P}{d^3} \propto V_P (SA_S)^3 \quad (4)$$

The fraction of new isolated particles, $x_{\Delta N_P}$, can then be calculated via SA_S at each cycling stage:

$$x_{\Delta N_P} = \frac{(N_P)_{Cycled} - (N_P)_{Fresh}}{(N_P)_{Cycled}} = \frac{(SA_S)_{Cycled}^3 - (SA_S)_{Fresh}^3}{(SA_S)_{Cycled}^3} \quad (5)$$

Fig. 7 shows the comparison between capacity loss calculated using eq. (5) using the measured surface area and the experimental capacity loss of each cell. For all room temperature samples, the calculated inactive new particle formation (used to estimate capacity loss) agreed well with the measured capacity loss. This result was consistent with previous results that particle fracture was one of the main degradation mechanisms for cells that cycled at room temperature. For the HT-Cell, new particle formation only contributed to approximately half of the capacity loss, further suggesting that another degradation mechanism, namely Mn dissolution as discussed previously, also played an important role.

4. Conclusions

In this study, transmission X-ray microscopy nanotomography was employed to quantitatively investigate LMO electrode 3D microstructural changes under different electrochemical cycling

conditions. Structural and chemical changes in electrode particles, including crack formation and material dissolution, respectively, were found after cycling. Microstructural parameters including specific surface area (SA_S) and particle size distributions (PSD_S) were extracted from tomography data to quantify structural changes. Statistical analysis of SA_S was used to assess the structural homogeneity and data accuracy, and proved that the observed SA_S increases after cycling were statistically significant. The increase of the SA_S was attributed to cracking during cycling, which quantitatively correlated to cell degradation by comparing the calculated capacity loss (based on SA_S) with measured data. Analysis of the PSD_S of all electrodes also showed a decrease in median particle size after cycling, which could be explained by crack formation during cycling. Finally, according to calculations based on the Griffith criterion, the critical fracture stress for crack extension for each cycling condition was also obtained, showing the consistent results with other simulations.

The quantitative analyses of the 3D electrode microstructures provided direct evidence to correlate the electrode microstructural changes and the cell degradation during cycling. For the cells operated under normal voltage and temperature conditions, both mechanical degradation and active material dissolution contributed to the capacity loss. The cracks were mainly induced by the stresses generated during repeated cycling during lithiation/delithiation. When the discharge voltage was lowered to 3 V, mechanical degradation contributed to the major capacity loss, as the onset of the Jahn-Teller distortion induced large stresses in the particles that resulted in crack formation. For the cell cycled at high temperature, microstructural changes yielded similar ΔSA_S with cells cycled under standard conditions. However, combining this result with EDS analysis, it can be concluded that enhanced Mn dissolution enhanced degradation of the HT cell.

Ex situ 3D quantitative microstructural analysis of electrodes as a function of cycle number, discharge voltage and temperature provides an efficient method to study degradation mechanisms of the electrode materials based on intercalation chemistry. Through this method, quantitative 3D images along with accurate electrochemistry information provide insight into the complex mechanical and electrochemical interactions in such electrode materials. By gaining this knowledge, it is expected that both robust electrode structures (e.g. optimized particle size, balancing between surface reaction and mechanical degradation) and cycling methods that limit electrochemical degradation (e.g. avoid large voltage cycling range that results in large stress generation within particle) can be developed, which will ultimately enable a rational strategy in designing better batteries.

Acknowledgement

The authors gratefully acknowledge financial support from the Office of Naval Research Grant #N00014-12-1-0713. Analysis and modeling of the data was partially supported as part of the Center for Electrochemical Energy Science, an Energy Frontier Research Center funded by the U.S. Department of Energy, Office of Science, Basic Energy Sciences. ZL acknowledges support from a Northwestern University Cabell Terminal Year Fellowship. SEM/EDS was performed in the EPIC facility of the NUANCE Center at Northwestern University. The NUANCE Center has received support from the Soft and Hybrid Nanotechnology Experimental (SHyNE) Resource (NSF ECCS-1542205); the MRSEC program (NSF DMR-1121262) at the Materials Research Center; the International Institute for Nanotechnology (IIN); the Keck Foundation; and the State of Illinois, through the IIN. The author also acknowledge Use of the National Synchrotron Light Source, BNL, was supported by the U.S. (DOE, BES), under Contract No. DE-AC02-98CH10886.

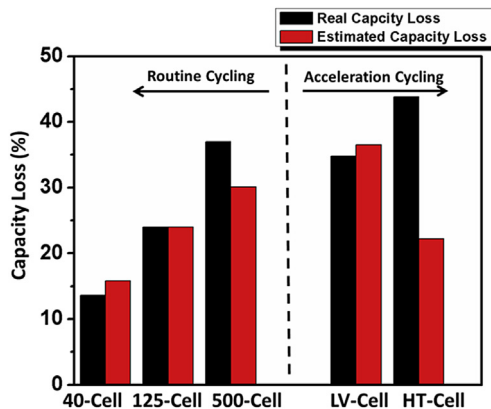


Fig. 7. Comparison between real capacity loss and calculated capacity loss of each cell.

Appendix A. Supplementary data

Supplementary data related to this article can be found at <http://dx.doi.org/10.1016/j.jpowsour.2017.06.027>.

References

- [1] P. Arora, R.E. White, *J. Electrochem. Soc.* 145 (1998) 3647–3667.
- [2] J. Vetter, P. Novak, M.R. Wagner, C. Veit, K.-C. Moller, J.O. Besenhard, M. Winter, M. Wohlfahrt-Mehrens, C. Vogler, A. Hammouche, *J. Power Sources* 147 (2005) 269–281.
- [3] Martin Winter, R.J. Brodd, *Chem. Rev.* 104 (2004) 4245–4269.
- [4] H. Wang, Y.-I. Jang, B. Huang, D.R. Sadoway, Y.M. Chiang, *J. Power Sources* 81–82 (1999) 594–598.
- [5] M.M. Thackeray, Y. Shao-Horn, A.J. Kahaian, K.D. Kepler, E. Skinner, J.T. Vaughey, S.A. Havkney, *Electrochem. Solid-State Lett.* 1 (1998) 7–9.
- [6] D. Liu, Y. Wang, Y. Xie, L. He, J. Chen, K. Wu, R. Xu, Y. Gao, *J. Power Sources* 232 (2013) 29–33.
- [7] D.H. Jang, Y.J. Shin, S.M. Oh, *J. Electrochem. Soc.* 143 (1996) 2204–2211.
- [8] M.J. Chon, V.A. Sethuraman, A. McCormick, V. Srinivasan, P.R. Guduru, *Phys. Rev. Lett.* 107 (2011).
- [9] W.H. Woodford, W.C. Carter, Y.-M. Chiang, *Energy & Environ. Sci.* 5 (2012) 8014.
- [10] W.H. Woodford, W.C. Carter, Y.M. Chiang, *J. Electrochem. Soc.* 161 (2014) F3005–F3009.
- [11] W.H. Woodford, Y.-M. Chiang, W.C. Carter, *J. Electrochem. Soc.* 157 (2010) A1052.
- [12] J.Y. Huang, L. Zhong, C.M. Wang, J.P. Sullivan, W. Xu, L.Q. Zhang, S.X. Mao, N.S. Hudak, X.H. Liu, A. Subramanian, H. Fang, L. Qi, A. Kushima, J. Li, *Science* 330 (2010) 1515–1520.
- [13] S.-H. Y, S.A. Hockney, A.J. Kahaian, K.D. Kepler, E. Skinner, J.T. Vaughey, M.M. Thackeray, *J. Power Sources* 81–82 (1999) 496–499.
- [14] P.R. Shearing, N.P. Brandon, J. Gelb, R. Bradley, P.J. Withers, A.J. Marquis, S. Cooper, S.J. Harris, *J. Electrochem. Soc.* 159 (2012) A1023–A1027.
- [15] Y.-c.K. Chen-Wiegart, Z. Liu, K.T. Faber, S.A. Barnett, J. Wang, *Electrochem. Commun.* 28 (2013) 127–130.
- [16] Z. Liu, J. Scott Cronin, Y.-c.K. Chen-Wiegart, J.R. Wilson, K.J. Yakal-Kremiski, J. Wang, K.T. Faber, S.A. Barnett, *J. Power Sources* 227 (2013) 267–274.
- [17] Z. Liu, Y.C. Chen-Wiegart, J. Wang, S.A. Barnett, K.T. Faber, *Microscopy and microanalysis : the official journal of microscopy society of America, microbeam analysis society, Microsc. Soc. Can.* 22 (2016) 140–148.
- [18] Z. Liu, T.J. Verhallen, D.P. Singh, H. Wang, M. Wagemaker, S.A. Barnett, *J. Power Sources* 324 (2016) 358–367.
- [19] P.R. Shearing, L.E. Howard, P.S. Jørgensen, N.P. Brandon, S.J. Harris, *Electrochem. Commun.* 12 (2010) 374–377.
- [20] K.J. Harry, D.T. Hallinan, D.Y. Parkinson, A.A. Macdowell, N.P. Balsara, *Nat. Mater.* 13 (2014) 71–73.
- [21] D.S. Eastwood, V. Yufit, J. Gelb, A. Gu, R.S. Bradley, S.J. Harris, D.J.L. Brett, N.P. Brandon, P.D. Lee, P.J. Withers, P.R. Shearing, *Adv. Energy Mater.* 4 (2013), 1300506.
- [22] J.B. Robinson, J.A. Darr, D.S. Eastwood, G. Hinds, P.D. Lee, P.R. Shearing, O.O. Taiwo, D.J.L. Brett, *J. Power Sources* 252 (2014) 51–57.
- [23] L. Zielke, T. Hutzenlaub, D.R. Wheeler, C.-W. Chao, I. Manke, A. Hilger, N. Paust, R. Zengerle, S. Thiele, *Adv. Energy Mater.* (2014) 1401612.
- [24] T. Hutzenlaub, S. Thiele, N. Paust, R. Spotnitz, R. Zengerle, C. Walchshofer, *Electrochimica Acta* 115 (2014) 131–139.
- [25] A.H. Wiedemann, G.M. Goldin, S.A. Barnett, H. Zhu, R.J. Kee, *Electrochem. Acta* 88 (2013) 580–588.
- [26] F. Tariq, V. Yufit, D.S. Eastwood, Y. Merla, M. Biton, B. Wu, Z. Chen, K. Freedman, G. Offer, E. Peled, P.D. Lee, D. Golodnitsky, N. Brandon, *ECS Electrochem. Lett.* 3 (2014) A76–A78.
- [27] J.N. Weker, N. Liu, S. Misra, J.C. Andrews, Y. Cui, M.F. Toney, *Energy & Environ. Sci.* 7 (2014) 2771.
- [28] M. Ebner, F. Marone, M. Stampanoni, V. Wood, *Science* 342 (2013) 716–720.
- [29] J. Wang, Y.C. Chen-Wiegart, J. Wang, *Angew. Chem.* 126 (2014) 4549–4553.
- [30] B. Lai, J. Nelson, Y. Yang, S. Misra, J.C. Andrews, Y. Cui, M.F. Toney, in: *Proceeding of SPIE*, vol. 8851, 2013, p. 88510B.
- [31] R. Scipioni, P.S. Jørgensen, D.-T. Ngo, S.B. Simonsen, Z. Liu, K.J. Yakal-Kremiski, H. Wang, J. Hjelm, P. Norby, S.A. Barnett, S.H. Jensen, *J. Power Sources* 307 (2016) 259–269.
- [32] H. Liu, J.M. Foster, A. Gully, S. Krachkovskiy, M. Jiang, Y. Wu, X. Yang, B. Protas, G.R. Goward, G.A. Botton, *J. Power Sources* 306 (2016) 300–308.
- [33] B. Song, T. Sui, S. Ying, L. Li, L. Lu, A.M. Korsunsky, *J. Mater. Chem. A* 3 (2015) 18171–18179.
- [34] M.S. Whittingham, *Chem. Rev.* 104 (2004) 4271–4301.
- [35] Y. Shao-Horn, Y. Ein-Eli, A.D. Robertson, W.F. Averill, S.A. Hockney, W.F.J. Howard, *J. Electrochem. Soc.* 145 (1998) 16–23.
- [36] T. Marks, S. Trussler, A.J. Smith, D. Xiong, J.R. Dahn, *J. Electrochem. Soc.* 158 (2011) A51.
- [37] M.M. Thackeray, W.I.F. David, P.G. Bruce, J.B. Goodenough, *Mat. Res. Bull.* 18 (1983) 461–472.
- [38] Y.C. Chen-Wiegart, F.E. Camino, J. Wang, *Chemphyschem a Eur. J. Chem. Phys. Phys. Chem.* 15 (2014) 1587–1591.
- [39] N. Otsu, *IEEE Trans. Syst. Man Cybern.* 9 (1979) 62–66.
- [40] M.D. Abramoff, P.J. Magalhães, S.J. Ram, *Biophot. Int.* 11 (2004) 36–42.
- [41] W.S. Rasband, *ImageJ*, U. S. National Institutes of Health, Bethesda, Maryland, USA, 1997–2016. <https://imagej.nih.gov/ij/>.
- [42] W.E. Lorensen, H.E. Cline, *Comput. Graph.* 21 (1987) 163–169.
- [43] B. Münch, L. Holzer, *J. Am. Ceram. Soc.* 91 (2008) 4059–4067.
- [44] J.C. Russ, *The Image Processing Handbook*, sixth ed., Taylor & Francis Group, LLC, 2011.
- [45] A. Blyr, C. Sigala, G. Amatuucci, D. Guymard, Y. Chabre, J.-M. Tarascon, *J. Electrochem. Soc.* 145 (1998) 194–209.
- [46] M.M. Thackeray, *Prog. Solid St. Chem.* 25 (1997) 1–71.
- [47] J. Christensen, J. Newman, *J. Electrochem. Soc.* 153 (2006) A1019.
- [48] M.M. Thackeray, *J. Electrochem. Soc.* 142 (1995) 2558–2563.
- [49] A.A. Griffith, *Philos. Trans. Royal Soc. Lond. Ser. A, containing papers of a mathematical or physical character* 221 (1921) 163–198.
- [50] R. Benedek, M.M. Thackeray, *Phys. Rev. B* 83 (2011) 195439.
- [51] J. Park, W. Lu, A.M. Sastry, *J. Electrochem. Soc.* 158 (2011) A201.
- [52] R. Purkayastha, R. McMeeking, *Comput. Mater. Sci.* 80 (2013) 2–14.